ELSEVIER

Contents lists available at ScienceDirect

Journal of Luminescence

journal homepage: www.elsevier.com/locate/jlumin



Full Length Article

Solventless mechanochemical synthesis of Sn-based halide perovskite microcrystals with high stability tracked by photoluminescence spectroscopy

Xuan Huang ^{a,b,1}, Xiaobing Tang ^{a,c,d,1}, Xiyu Wen ^e, Y. Charles Lu ^{a,b,**}, Fuqian Yang ^{a,d,*}

- ^a Laboratory of Functional Materials, University of Kentucky, Lexington, KY, 40506, USA
- b Department of Mechanical and Aerospace Engineering, University of Kentucky, Lexington, KY, 40506, USA
- ^c School of Mechanical Engineering, University of Shanghai for Science and Technology, Shanghai, 200093, PR China
- d Materials Program, Department of Chemical and Materials Engineering, University of Kentucky, Lexington, KY, 40506, USA
- ^e Center for Aluminium Technology, University of Kentucky, Lexington, KY, 40506, USA

ARTICLE INFO

Keywords: Tin-based lead-free perovskites Mechanochemistry Phase transformation Long-term stability

ABSTRACT

Developing solvent-free methods to synthesize lead-free perovskites is of practical importance from the viewpoint of sustainability. In this work, we use a facile mechanochemical approach to synthesize a series of lead-free Sn-based halide perovskite microcrystals (powders) in ambient conditions directly from precursor powders (CsX and SnX₂ (X = I, Br, Cl)) without any solvent. Such an approach is energy-saving and avoids the use of toxic solvents. There exists phase evolution during the mechanochemical processing of the precursor powders with $CsSn_2Br_5$ to $CsSnBr_3$ in the first hour and finally into the stabilized phase of Cs_2SnE_6 after 28 days and with Cs_2SnCl_4 to $CsSnCl_3$ in the first hour and finally to the stabilized phase of Cs_2SnCl_6 after 36 days. The stabilized Cs_2SnI_6 powders emit light centered at 930 nm under the excitation of 785 nm, and the stabilized Cs_2SnI_6 powders emit light centered at 682 nm under the excitation of 365 nm. Both the stabilized Cs_2SnI_6 and Cs_2SnI_6 powders exhibit excellent long-term structural and optical stabilities, and the Cs_2SnI_6 powders have a better thermal stability than the Cs_2SnI_6 powders. This work likely offers a green-route synthesis of lead-free halide perovskites towards large-scale manufacturing and industrialization.

1. Introduction

Lead-halide perovskites, as semiconductor materials with potential applications in optoelectronics and next-generation photovoltaic cells, have attracted great interest due to the low cost in the facile solution-based synthesis processes and their unique optoelectronic characteristics of tunable visible-spectrum wavelength and narrow full width at half maximum (FWHM) [1,2], high optical absorption, large diffusion length of charge carriers and good defect resistance. Both inorganic and organometallic lead-halide perovskites of APbX₃ (A = Cs, MA, FA and X = Cl, Br, I with MA for methylammonium and FA for formamidinium) bulk materials [3–5] and their nano-counterparts [6,7] have been demonstrated successfully in the applications of light emitting diodes (LEDs) [8], quantum-dot light emitting diodes (QLEDs) [9–11] and photovoltaic cells. However, the toxicity of Pb in PbX₂ as a product from

the degradation of APbX₃ [12] has raised concerns about the applications of APbX₃ in optoelectronics and bioimaging, and likely impedes the commercialization and industrialization of lead-halide perovskites.

There is a great need to produce environmental-friendly perovskites with excellent optoelectronic properties. For examples. Wei et al. [13] prepared Na $^+$ -doped Cs₂SnI $_6$ nanocrystals with orange emission. Zhou et al. [14] obtained air stable Sb $^{3+}$ -doped (C₈H₂₂N₂Cl)₂SnCl $_6$ with the emission peak centered at 690 nm. Ma et al. [15] constructed stable white light-emitting diodes from a copper-based composite with CsCu₂I₃@Cs₃Cu₂I₅. Zhang et al. [16] synthesized millimeter Cs₃Cu₂I₅ crystals with blue emission. Using electrospinning technique, Jiang et al. [17] prepared poly(vinylidene fluoride) fibers with Cs₃Cu₂I₅ nanocrystals. Xie et al. [18] obtained Cs₃Cu₂X₅ (X = I, Cl) perovskites with blue and green emissions, respectively. Tin-based perovskites with promising optical properties avoid the lead toxicity from the

^{*} Corresponding author. Materials Program, Department of Chemical and Materials Engineering, University of Kentucky, Lexington, KY, 40506, USA.

^{**} Corresponding author. Department of Mechanical and Aerospace Engineering, University of Kentucky, Lexington, KY, 40506, USA. *E-mail addresses*: ycharles.lu@uky.edu (Y.C. Lu), fuqian.yang@uky.edu (F. Yang).

 $^{^{1}\,}$ X.H. and X.T. contributed equally to this work.

degradation of lead-based halide perovskites and have the potential to replace lead-based halide perovskites in the applications of optoelectronics and next-generation photovoltaic cells. The synthesis methods of tin-based perovskites can be grouped into two categories: solution-based methods [19] and thermal evaporation [20]. The solution-based methods generally require the use of toxic-organic solvents, such as dimethylformamide (DMF) and dimethyl sulfoxide (DMSO) [21] in the precursor solutions and octadecene (ODE) in a hot injection process [22], which are a threat to the environment. Also, the high temperature and inert gases used in the hot injection process make it a complex and high-cost process for the synthesis of tin-based perovskites (as well as lead-based perovskites). To limit the use of toxic-organic solvents, hydrothermal process with aqueous solution was developed [23], which, however, still involves the use of high pressure and high temperature in the synthesis. Thermal evaporation [24] without solvents has been considered as an environmental-friendly method, while the high temperatures needed for the evaporation of raw materials make it a high energy-consuming approach [25,26].

Mechanochemical (MC) synthesis, which is attributed to chemical reactions induced by mechanical energy, converts externally imposed strain energy in "bulk" materials to chemical energy to achieve the formation of new solid phases of smaller sizes [27]. The paths available for MC synthesis include grinding, ball milling and other similar processing of powders [28], among which grinding is the simplest engineering technique [28,29]. MC synthesis has been recognized as a green route without hazardous solvents to produce materials of submicron and nanosizes and has been successfully used in the synthesis of lead-based perovskites [30-32]. However, there are few reports on the MC processing of lead-free perovskites. Hong et al. [33] prepared CsSnX₃ (X = I, Br, Cl) and mixed halide perovskites through a ball-milling approach. Ajjouri et al. [34] reported a ball-milling method for the synthesis of perovskites including inorganic, organic-inorganic hybrid and double perovskites. However, these works did not report and discuss the phase formation/transformation during the MC processes. Also, the MC approaches used in these works involved the use of high energy and an inert-gas atmosphere, which likely results in a complex and high-cost path for the preparation of perovskites. Another MC method available for the processing of halide perovskites is resonant-acoustic mixing, which requires disposable powders during the specimen preparation and likely causes a waste of materials and an increase of cost [35].

The aim of this work is to demonstrate the feasibility of the MC processing of tin-based halide microcrystals (powders). Instead of using a ball-milling machine and/or an ultrasonicator, a manually controlled MC method (manual grinding in a ceramic mortar) was used to produce Cs_2SnI_6 , $CsSnBr_3$ and $CsSnCl_3$ powders. The evolution of solid phases from the precursor powders during the processing was monitored. The crystal structures and photoluminescence of the prepared Cs_2SnI_6 , $CsSnBr_3$ and $CsSnCl_3$ powders were characterized. The chemical reactions to form Cs_2SnI_6 , $CsSnBr_3$ and $CsSnCl_3$ were presented. The stabilities of the as-prepared Cs_2SnI_6 , Cs_2SnBr_6 , and Cs_2SnCl_6 in the air were also discussed.

2. Experimental details

The chemicals used in this work were cesium iodide (99.9%, Alfa Aesar), cesium bromide (99.9%, Beantown chemical), cesium chloride (99.9%, Alfa Aesar), tin (II) iodide (99%, Strem Chemical), tin (II) bromide (99%, Beantown chemical), and tin (II) chloride (99%, Sigma Aldrich). They were used as received without further purification.

Figure S1 (Supplementary Information) shows schematically the MC processing of SnX_2 and CsX to form Cs_2SnX_6 and/or $CsSnX_3$. Briefly, the mixture of equimolar SnX_2 and CsX powders (0.4 mmol each) was placed in a ceramic mortar at room temperature. A ceramic pestle was used to manually ground the mixture in the mortar at room temperature in the air. It is noted that the material synthesis is significantly dependent on the synthesis temperature and humidity [36,37]. The

temperature and humidity were 19 $^{\circ}$ C and 60%, respectively, during the grinding. The grinding time was 30 min for the preparation of Cs₂SnI₆ powders and 1 h for the preparation of CsSnBr₃ and CsSnCl₃ powders.

The prepared powders were analyzed on an X-ray diffractometer (XRD) (Siemens D500) with a radiation of CuK_{α} ($\lambda=1.5406\ \text{Å}$). The morphologies of the as-obtained powders were analyzed on a scanning electron microscope (SEM) (JSM-I T700HR) equipped with an integrated energy dispersive X-ray (EDS) detector. The surface chemistry of the as-prepared specimens was investigated on a K-Alpha X-ray photoelectron spectrometer (XPS) (Thermal Scientific). Photoluminescent (PL) characteristics of the prepared powders were determined on a spectrometer (Ocean Optics) with three excitation wavelengths of 365, 405 and 785 nm under the same operation conditions. A UV–Visible spectrophotometer (Thermo Scientific Evolution) was used to measure the UV–Vis absorbance of the prepared powders.

3. Calculations of molar fraction

The molar fractions of the formed perovskite compounds were calculated by analyzing the corresponding XRD spectra. Briefly, let A and B represent two materials in a mixture. The mass ratio between A and B is equal to the ratio of the corresponding XRD peak intensity. The corresponding molar ratio is calculated as n(A):n(B) = (m(A)/M(A)):(m(B)/M(B)) (m and M are the mass and molar mass, respectively), and the molar fractions of A and B are calculated as n(A)/(n(A) + n(B)) and n(B)/(n(A) + n(B)), respectively.

4. Results and discussion

Fig. 1a presents the XRD pattern of the as-prepared powders from SnI2 and CsI powders. The XRD pattern matches well with the JCPDS card (PDF#025-0743) of cubic Cs₂SnI₆, confirming that the mechanical grinding of the mixture of SnI2 and CsI powders mainly led to the formation of cubic Cs₂SnI₆. The cubic structure of Cs₂SnI₆ powders with space group of Fm3m is in coincidence with the results reported in the literature [38–40]. The XRD peaks centered at 13.2° , 15.3° , 21.6° , 25.3° , 25.6°, 30.7°, 34.3°, 37.9°, 40.3°, 44.1°, 52.2° and 54.7° correspond, respectively, to (111), (200), (220), (311), (222), (400), (420), (422), (511), (440), (622) and (444) crystal planes of cubic Cs₂SnI₆. Fig. 1b shows a 3D crystal structure of the cubic Cs₂SnI₆. The insets in Fig. 1b are optical images of the as-prepared Cs₂SnI₆ powders under white light (WL) (top) and ultraviolet (UV) light (bottom). There is no observable difference in the colors of the as-prepared Cs₂SnI₆ powders under WL and UV light, suggesting that the powders do not emit visible light under UV light.

The formation of Cs_2SnI_6 during the grinding of the mixture of SnI_2 and CsI powders can be attributed to the following chemical reaction associated with the role of O_2 in the air under mechanical grinding

$$2CsSnI_3 + O_2 \rightarrow Cs_2SnI_6 + SnO_2 \tag{1}$$

The XRD pattern of SnO_2 presented in Fig. 1a is in accord with the JCPDS card (PDF# 97-005-6674). It should be noted that the impurity of SnI_4 in the reactant can also lead to the formation of Cs_2SnI_6 . In cubic Cs_2SnI_6 crystal, the octahedra $[SnI_6]^{2-}$ with Sn^{4+} and eight I^- is coordinated with Cs^+ . Comparing with cubic $CsSnI_3$ crystal, cubic Cs_2SnI_6 crystal can be regarded as cubic double perovskite ($A_2B^*BX_6$) with the B'-site atom being occupied by a vacancy. Thus, Cs_2SnI_6 can be represented by A_2BX_6 and called as vacancy-ordered double perovskite [40].

Fig. 1c depicts the XRD pattern of the freshly prepared powders from SnBr $_2$ and CsBr powders. The XRD peaks centered at 21.8°, 26.7°, 31.0°, 34.5°, 38.1°, 44.4°, 49.9°, 52.4°, 55.0° and 59.6° correspond, respectively, to (110), (111), (200), (210), (211), (220), (310), (311), (222) and (321) crystal planes of cubic CsSnBr $_3$ and match well with the JCPDS card (PDF#000–4071). This result reveals that the mechanical grinding of the mixture of equimolar SnBr $_2$ and CsBr powders mainly led

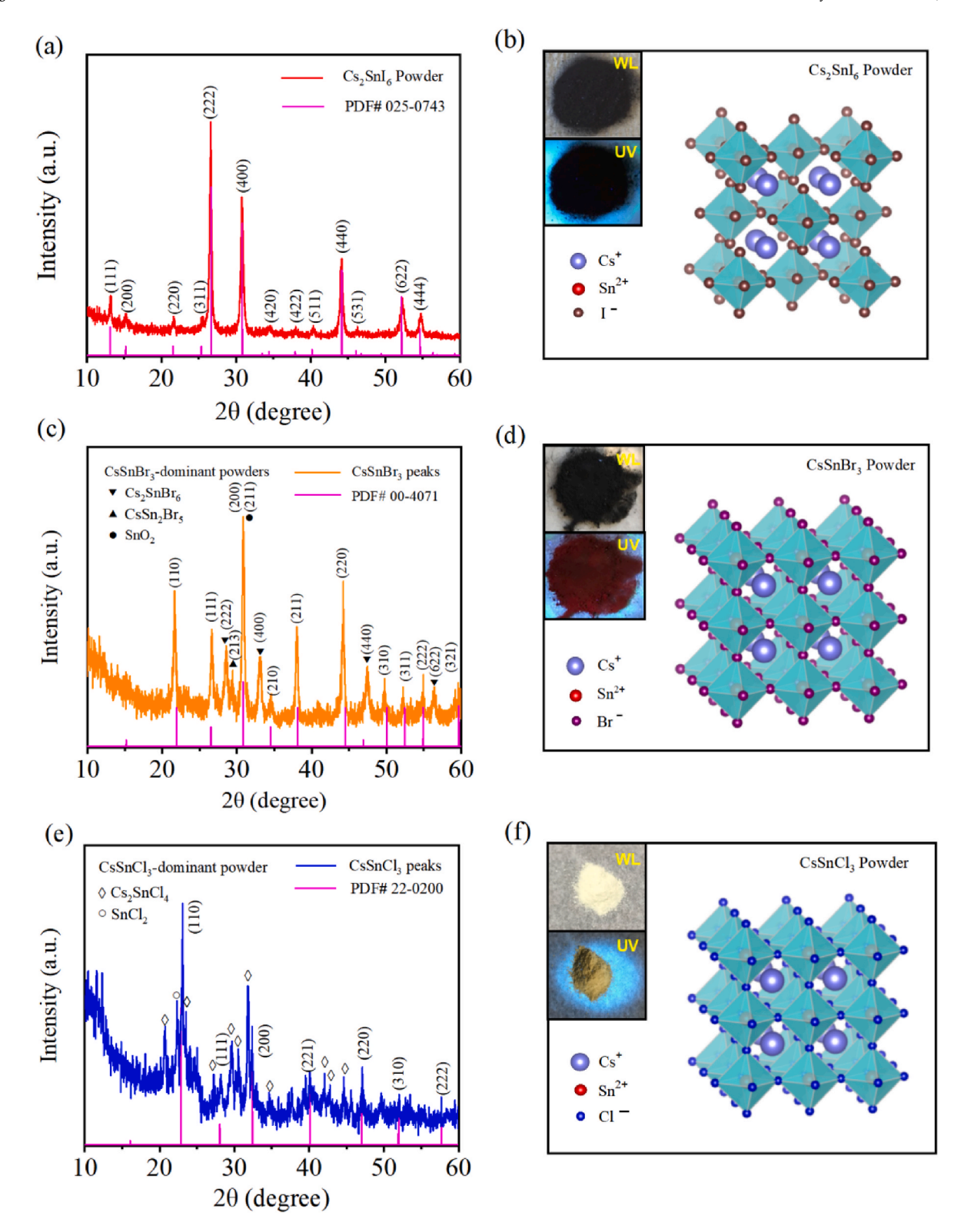


Fig. 1. XRD patterns of freshly prepared Cs_2SnI_6 powders (a), $CsSnBr_3$ -dominated powders (c), and $CsSnCl_3$ -dominated powders (e). The corresponding crystal structures of Cs_2SnI_6 , $CsSnBr_3$, and $CsSnCl_3$ are presented in (b), (d) and (f), respectively. (Insets are optical images of the respective powders under white light (WL) and ultraviolet (UV) light.).

to the formation of cubic CsSnBr₃ (Fig. 1d) with a space group of $Pm\overline{3}m$, which is different from the formation of cubic Cs₂SnI₆ crystal from the mechanical grinding of the mixture of equimolar SnI₂ and CsI powders.

Note that the XRD pattern also reveals the presence of small amounts of Cs_2SnBr_6 and $CsSn_2Br_5$ (see details about the formation of the two

chemicals hereinafter) in the final product, as illustrated by the XRD peaks. The (220), (222), (400), (440) and (622) crystal planes of cubic Cs_2SnBr_6 (JCPDS card (PDF#97-015-8957)) are represented by solid black down-pointing triangles, and the (213) crystal plane of $CsSn_2Br_5$ (JCPDS card (PDF# 97-009-3792)) is represented by a solid black up-

pointing triangle for the XRD peak centered at 29.33° . Note that the XRD peak for the (200) plane of Cs_2SnBr_6 overlaps with the XRD peak for the (211) plane of SnO_2 according to the JCPDS card (PDF# 97-018-1280)), which likely suggests the formation of Cs_2SnBr_6 from $CsSnBr_3$. The formation of Cs_2SnBr_6 and $CsSn_2Br_5$ can be described by the following chemical reactions of (2) and (3), respectively.

$$2CsSnBr_3 + O_2 \rightarrow Cs_2SnBr_6 + SnO_2$$
 (2)

$$CsBr + 2SnBr_2 \rightarrow CsSn_2Br_5 \tag{3}$$

Equation (3) indicates that there exists a small residual of CsBr after the mechanical grinding and the superfluous CsBr should be presented in the as-prepared powders. However, there are no XRD peaks of CsBr in Fig. 1c, likely due to the measurement limitation of the XRD instrument. The XRD results indicate that the as-prepared Sn-based perovskite powders are a mixture of CsSnBr₃, Cs₂SnBr₆, and CsSnBr₅ with the dominance of cubic CsSnBr₃. The insets in Fig. 1d present optical images of the as-prepared CsSnBr₃-dominated powders under WL (top) and UV light (bottom). It is evident that the as-prepared CsSnBr₃-dominated powders exhibit red emission under the UV light. The unit cell of the cubic CsSnBr₃ crystal consists of an octahedra [SnBr₆]⁴⁻ and eight Cs⁺ co-shared with eight-unit cells.

Most peaks in the XRD pattern shown in Fig. 1e for the freshly prepared powders from SnCl₂ and CsCl powders match well with the JCPDS card (PDF#022–0200), suggesting that the as-prepared powders mainly consist of CsSnCl₃ of cubic structure. The XRD peaks centered at 22.5°, 28.1°, 31.9°, 40.2°, 47.3°, 52.1° and 57.1° correspond, respectively, to (110), (111), (200), (221), (220), (310) and (222) crystal planes of cubic CsSnCl₃. According to Fig. 1e, there is a small amount of Cs₂SnCl₄ presented in the as-prepared powders. The corresponding XRD peaks are represented by open diamonds and match well with tetragonal Cs₂SnCl₄ [41] (JCPDS card (PDF#28–0346)). This result reveals that the as-prepared powders are a mixture of CsSnCl₃ and Cs₂SnCl₄. The chemical reaction for the formation of Cs₂SnCl₄ can be illustrated as below

$$2CsCl + SnCl_2 \rightarrow Cs_2SnCl_4 \tag{4}$$

Similar to the formation of the $CsSnBr_3$ -dominated powders, equation (4) indicates that there is a small residual of $SnCl_2$ in the as-prepared $CsSnCl_3$ -dominanted powders. This is supported by the XRD peak represented by an open circle in Fig. 1e. The insets in Fig. 1f show optical images of the as-prepared $CsSnCl_3$ -dominanted powders under WL (top) and UV light (bottom). It is evident that there is coffee-light emission from the cubic $CsSnCl_3$ -dominanted powders under the UV light.

SEM imaging was carried out to observe the morphologies of the asprepared powders. Figures S2 in Supplementary Information present typical SEM images of the as-obtained powders. The Cs_2SnI_6 powders are presented in a cube-like shape with an average size of $\sim\!350$ nm. Both the $CsSnBr_3$ -dominated powders and $CsSnCl_3$ -dominated powders are presented in an irregular shape.

The EDS spectra of the as-prepared powders are shown in Figs. S3 in Supplementary Information. The atomic ratios of Cs:Sn:I, Cs:Sn:Br, and Cs:Sn:Cl are calculated to be around 2:1:6, 1:1:3, and 1:1:3, respectively. The results support the formation of Cs_2SnI_6 , $CsSnBr_3$, and $CsSnCl_3$ from the grinding of the corresponding precursor powders.

The surface chemistry of the as-prepared powders was investigated by X-ray photoemission spectroscopy. The XPS spectrum (Fig. S4b in Supplementary Information) of $\rm Cs_2SnI_6$ shows characteristic peaks of Sn $\rm 3d_{5/2}$ and $\rm 3d_{3/2}$ at 487.2 and 495.7 eV, respectively. The characteristic peaks of Sn $\rm 3d_{5/2}$ and $\rm 3d_{3/2}$ for CsSnBr $_3$ (Fig. S4d in Supplementary Information) are centered at 487.0 and 495.3 eV, respectively. It is evident that the Sn $\rm 3d_{5/2}$ of $\rm Cs_2SnI_6$ is larger than that of CsSnBr $_3$ due to that the Sn $^{4+}$ of Cs $_2\rm SnI_6$ has a larger binding energy than the Sn $^{2+}$ of CsSnBr $_3$ [42]. The characteristic peaks of Sn $\rm 3d_{5/2}$ and $\rm 3d_{3/2}$ of CsSnCl $_3$ (Fig. S4f in Supplementary Information) are the same as the

corresponding ones of $CsSnBr_3$, attributed to Sn^{2+} in both the materials. These results are in accord with the reports in the literature [39,43]. The XPS results are qualitatively in accordance with the EDS results shown in Fig. S2.

The presence of the Cs₂SnBr₆ and Cs₂SnCl₄ in the as-prepared powders from the respective grinding of the mixture of SnBr2 and CsBr powders and the mixture of SnCl₂ and CsCl powders suggests that there likely exist phase evolutions between CsSnBr3 and Cs2SnBr6 and between CsSnCl₃ and Cs₂SnCl₄ during the grinding. We further analyze the structures of the as-prepared powders from the ground mixture of SnBr2 and CsBr powders and the ground mixture of SnCl2 and CsCl powders, respectively, at different instants. Fig. 2 presents the XRD patterns of the as-prepared powders from the ground mixture of SnBr2 and CsBr powders (Fig. 2a) and the ground mixture of SnCl2 and CsCl powders (Fig. 2b) at different instants. The XRD patterns in Fig. 2a reveal the presences of CsSn₂Br₅ (JCPDS card (PDF#09-3792)) represented by solid black up-pointing triangles and CsSnBr3 (JCPDS card (PDF#00-4071)) represented by open triangles after 10 min grinding. Further grinding to 1 h led to a significant increase in the amount of CsSnBr3, a dramatic decrease in the amount of CsSn2Br5 and the formation of a small portion of Cs₂SnBr₆ (JCPDS card (PDF#15-8957)). More details on the evolution of the individual phases are presented in Fig. S5a (Supplementary Information). Table S1 (Supplementary Information) summarizes the variations of the molar fractions of CsSn₂Br₅, Cs₂SnBr₆ and CsSnBr₃ with the grinding time, which are calculated from the XRD results. The molar fraction of CsSn₂Br₅ decreases gradually from 71.27% to 57.49% with increasing the grinding time from 10 min to 20 min, while the molar fraction of CsSnBr₃ increases from 28.73% to 42.51%. These results indicate that both CsSn₂Br₅ and CsSnBr₃ were formed from the mixture of the precursor powders of CsBr and PbBr₂ after the grinding of 10 min. The main product is CsSn₂Br₅, and further grinding caused the reaction between CsSn2Br5 and CsBr to form CsSnBr₃. Cs₂SnBr₆ with a molar fraction of 7.84% appeared after the grinding time reached 30 min. The molar fraction of Cs₂SnBr₆ continues to increase to 17.25% with increasing the grinding time to 60 min. Simultaneously, the molar fraction of CsSn₂Br₅ decreases from 17.58% to 11.56% and the molar fraction of CsSnBr3 remains almost unchanged for the grinding time between 30 min and 60 min. This trend suggests that the formation of Cs₂SnBr₆ is mainly controlled by the CsSn₂Br₅ for the grinding time between 30 min and 60 min. It should be noted that the atomic ratio of Cs to Sn to Br in the mixed powders (CsSnBr₃, CsSn₂Br₅ and Cs₂SnBr₆) remains close to 1:1:3, indicating the mass conservation during this grinding time.

According to Fig. 2a, the mixture of CsSnBr₃, CsSn₂Br₅ and Cs₂SnBr₆ evolved finally to the stabilized phase of Cs₂SnBr₆ with a small fraction of SnO2 after 28 days. Note that there is an insignificant shift towards small diffractive angles for the XRD peaks of Cs₂SnBr₆ comparing with the corresponding JCPDS card (PDF#15-8957), which is likely attributed to internal stress in the Cs₂SnBr₆ crystals. Fig. S5b (Supplementary Information) shows the evolution of the XRD pattern, from which the molar fractions of the individual phases in the mixture are calculated and listed in Table S2 (Supplementary Information). The molar fractions of CsSn₂Br₅ and CsSnBr₃ decrease respectively from 16.27% and 43.66% after the first week to 0% and 0%, respectively, after the fourth week, and the molar fractions of Cs₂SnBr₆ and SnO₂ (JCPDS card PDF#97-019-1345) increase respectively from 40.07% and 0% to 48.93 % and 51.07 %, respectively, within the same period. This indicates that both CsSnBr₃ and CsSn₂Br₅ contributed to the formation of Cs₂SnBr₆. Using the molar fractions, we calculate the atomic ratios of elements in the mixtures at different instants (week 1 to week 4) and find that the atomic ratio of Cs to Sn to Br remains to be 1 to 1 to 3 approximately, corresponding to the atomic ratio of the elements in the raw materials (CsBr and SnBr₂) powders). All these results reveal the presence of the phase evolution from the freshly prepared CsSnBr3 with CsSn2Br5 and Cs2SnBr6 to Cs₂SnBr₆ and SnO₂, i.e., CsSnBr₃ and CsSn₂Br₅ react in the air to form Cs₂SnBr₆ and SnO₂ in ambient conditions.

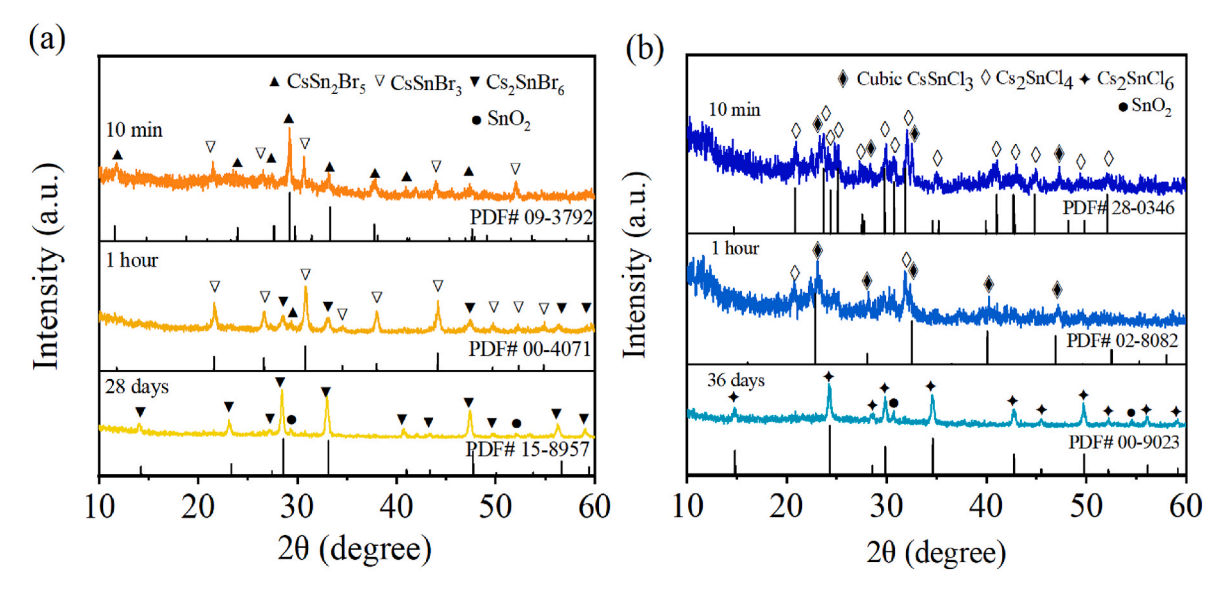


Fig. 2. XRD patterns of the as-prepared CsSnBr₃-dominated and CsSnCl₃-dominated powders at different instants, showing the presence of phase evolution: (a) CsSnBr₃ (phase evolution from CsSnBr₃ to Cs₂SnBr₆), and (b) CsSnCl₃ (phase evolution from CsSnCl₃ to Cs₂SnCl₆).

Figs. 2b and S5c (Supplementary Information) depict the XRD patterns of the freshly prepared powders from SnCl₂ and CsCl powders, which consists of CsSnCl₃ powder (JCPDS card (PDF#02-8082)) represented by solid diamonds and Cs2SnCl4 powder (JCPDS card (PDF#28-0346)) represented by open diamonds, under the grinding of 1 h. Using the XRD patterns, the molar fractions of Cs₂SnCl₄ and CsSnCl₃ are calculated and listed in Table S3 (Supplementary Information). Note that the molar fractions of Cs₂SnCl₄ and CsSnCl₃ are about the same after the first 10 min grinding. Further increasing the grinding time to 60 min led to the increase of the molar fraction of CsSnCl3 and the decrease of the molar fraction of Cs₂SnCl₄. This result suggests that both Cs₂SnCl₄ and CsSnCl3 are likely formed simultaneously at the beginning of the grinding. Further grinding caused the decrease of the molar fraction of Cs₂SnCl₄ from 49.22% to 36.63% and the increase of the molar fraction of CsSnCl₃ from 50.78% to 63.37% after 60 min grinding. This trend indicates that there exists a reaction between SnCl2 and Cs2SnCl4 to form CsSnCl₃ during the grinding. Note that the insignificant shifts of the XRD peaks to big diffractive angles for both Cs2SnCl4 and CsSnCl3 are likely due to the internal stress in the crystals. Similar to the evolution of CsSnBr₃, the as-resulted CsSnCl₃ reacted with O₂ to form the stabilized phase of Cs₂SnCl₆ (JCPDS card (PDF#00-9023)) after 36 days in ambient conditions. The evolution of the XRD pattern is presented in Fig. S5d (Supplementary Information), and the evolutions of the molar fractions of the Cs₂SnCl₄ and CsSnCl₃ are listed in Table S4 (Supplementary Information). Both the molar fractions of Cs₂SnCl₄ and CsSnCl₃ remain almost unchanged for the first two weeks. After the third week, both the molar fractions of Cs₂SnCl₄ and CsSnCl₃ decrease (32.71% and 50.94% for Cs₂SnCl₄ and CsSnCl₃, respectively, after the third week and 0.00% and 0.00% for Cs₂SnCl₄ and CsSnCl₃, respectively, after the fifth week). In the same period (third week to fifth week), the molar fraction of Cs₂SnCl₆ increases from 16.35% to 49.42%, and the molar fraction of SnO₂ (JCPDS card PDF#97-016-9034) increases from 42.43% after the fourth week to 50.58% after the fifth week. Both Cs₂SnCl₄ and CsSnCl₃ contributed to the formation of Cs₂SnCl₆. The atomic ratio of Cs to Sn to Cl in the prepared powders remains approximately to be 1:1:3 for Cs:Sn: Cl in accord with the atomic ratio of the raw materials of CsCl and SnCl₂ powders, which implies the mass conservation during the phase evolution. These results suggest that the grinding of CsCl and SnCl2 powders can lead to the formation of CsSnCl3 and Cs2SnCl4, which react to form Cs₂SnCl₆ and SnO₂ in ambient conditions.

According to the XRD patterns shown in Figs. 2 and S5 (Supplementary Information) and Table S1-S4 (Supplementary Information),

the chemical reactions associated with the formation of new phases are summarized below and shown schematically in Fig. 3.

$$CsBr + 2SnBr_2 \rightarrow CsSn_2Br_5$$
 (5)

$$CsBr + SnBr_2 \rightarrow CsSnBr_3 \tag{6}$$

$$CsSn_2Br_5 + CsBr \rightarrow 2CsSnBr_3 \tag{7}$$

$$2CsSnBr_3 + O_2 \rightarrow Cs_2SnBr_6 + SnO_2$$
 (8)

$$CsSn2Br5 + CsBr + O2 \rightarrow Cs2SnBr6 + SnO2$$
(9)

$$CsCl + SnCl_2 \rightarrow CsSnCl_3$$
 (10)

$$2CsCl + SnCl_2 \rightarrow Cs_2SnCl_4$$
 (11)

$$Cs_2SnCl_4 + SnCl_2 \rightarrow 2CsSnCl_3$$
 (12)

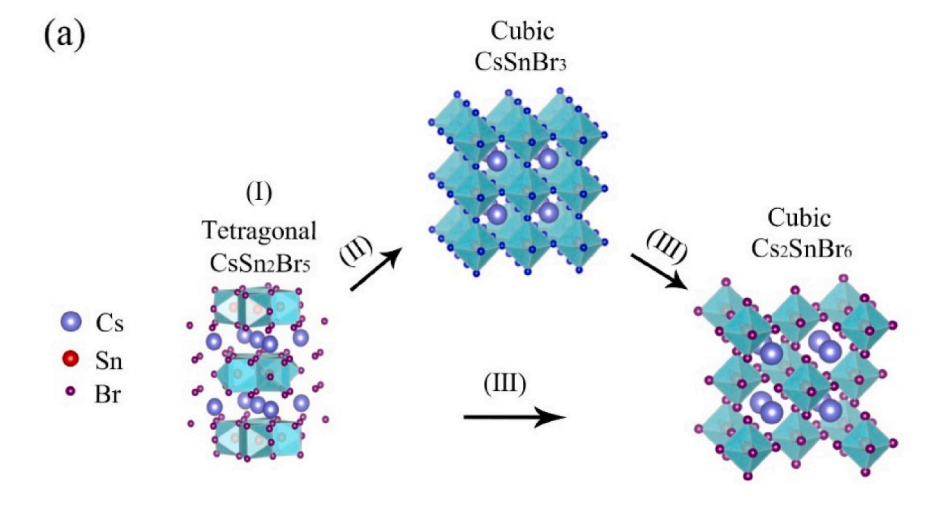
$$2CsSnCl_3 + O_2 \rightarrow Cs_2SnCl_6 + SnO_2$$
 (13)

$$Cs_2SnCl_4 + SnCl_2 + O_2 \rightarrow Cs_2SnCl_6 + SnO_2$$
 (14)

Fig. 3a shows the paths to form cubic Cs_2SnBr_6 from CsBr and $SnBr_2$. Mechanically grinding CsBr and $SnBr_2$ leads to the formation of tetragonal $CsSn_2Br_5$ (stage I) and cubic $CsSnBr_3$ (small fraction) initially. The as-formed $CsSn_2Br_5$ is not stable and reacts with residual CsBr to form more cubic $CsSnBr_3$ (stage II). Under the ambient condition, both $CsSn_2Br_5$ and $CsSnBr_3$ are oxidized to form cubic Cs_2SnBr_6 (stage III).

Fig. 3b shows the paths to form cubic Cs₂SnCl₆ from CsCl and SnCl₂. Mechanically grinding CsCl and SnCl₂ leads to the formation of tetragonal Cs₂SnCl₄ and cubic CsSnCl₃ initially (stage I). The as-formed Cs₂SnCl₄ then reacts with residual SnCl₂ to forms more cubic CsSnCl₃ (stage II). Under the ambient condition, both Cs₂SnCl₄ and CsSnCl₃ are oxidized to form cubic Cs₂SnCl₆ (stage III).

Fig. 4a and c presents the PL spectra of the as-prepared Cs_2SnI_6 and $CsSnBr_3$ -dominated powders under the excitation of 785 and 405 nm, respectively. The Cs_2SnI_6 powders exhibit a PL peak centered at \sim 930 nm, corresponding to a band gap of \sim 1.33 eV in consistence with 1.3 eV reported in the literature [38]. The $CsSnBr_3$ -dominated powders exhibit a PL peak centered at \sim 691 nm under the excitation of 405 nm, which is in consistence with the results reported in the literature [33,44,45]. Note that the broad band of the PL peak centered at \sim 691 nm can be attributed to a large range of the particle (microcrystal) sizes of the as-prepared $CsSnBr_3$ -dominated powders. The absorbance spectra of the as-prepared $Cs2SnI_6$ and $CsSnBr_3$ -dominated powders are presented in



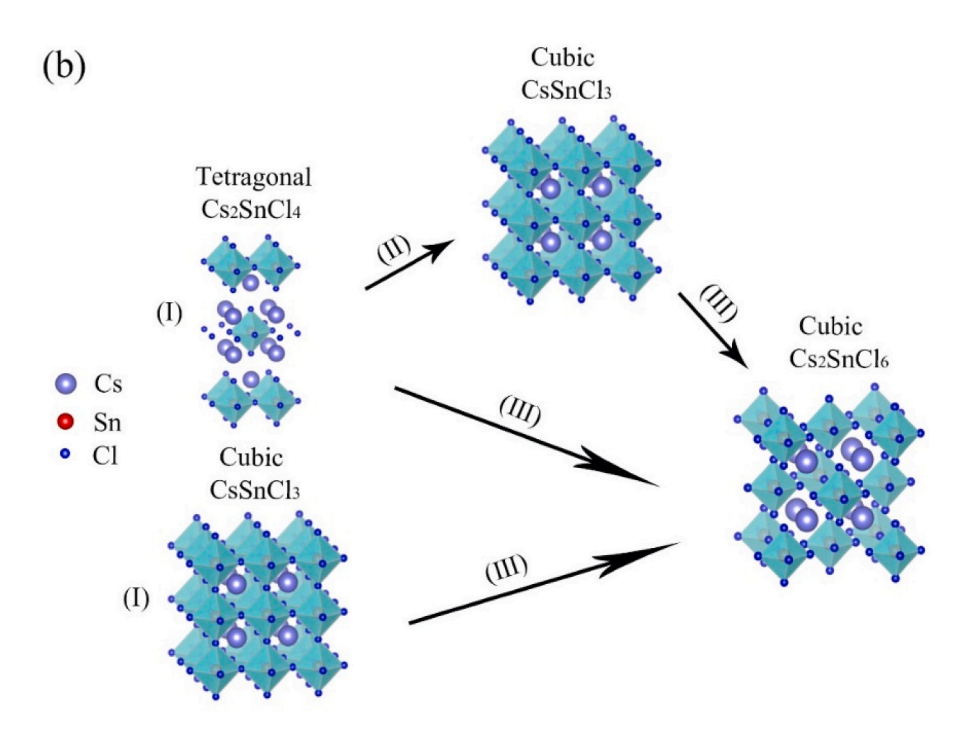


Fig. 3. Schematic of phase evolutions: (a) CsSn₂Br₅ to Cs₂SnBr₆, and (b) Cs₂SnCl₄ and CsSnCl₃ to Cs₂SnCl₆.

Fig. 4b and d, respectively. Using the absorbance data, the Tauc plots are constructed and inserted in the corresponding figures. From the Tauc plots, we obtain the bandgaps of 1.72~eV for the as-prepared Cs_2SnI_6 in agreement with the result given by Qiu et al. [46] and 1.85~eV for the as-prepared Cs_2SnB_3 , respectively. Both the bandgaps determined from the absorbance spectra are larger than the corresponding ones determined from the PL spectra.

It is interesting to note that there are multiple PL peaks centered at 435, 488, 586, 543 and 612 nm for the as-prepared $CsSnCl_3$ -dominated powders under UV light of 365 nm in wavelength, as shown in Fig. 4e. The mechanism for such behavior is unclear. It might be due to that there exists recombination of holes and electrons in multiple sub-bands [47]. Fig. 4f depicts the absorbance spectrum of the as-prepared $CsSnCl_3$ -dominated powder, from which a bandgap of 2.57 eV is obtained from the corresponding Tauc plot (the inset in Fig. 4f). Note that the value of 2.57 eV is slightly smaller than \sim 2.98 eV reported in the literature [33,44,45]. This can be likely attributed to the presence of

 Cs_2SnCl_4 in the $CsSnCl_3$ -dominated powders. The former possesses a bandgap in a range of $\sim 1.20-1.51$ eV [41].

For the purpose of comparison, we re-synthesized the materials $(Cs_2SnI_6, CsSnBr_3)$ and $CsSnCl_3$ powders) at a humidity of 40% with the grinding times of ~ 35 min for the mixture of CsI and SnI_2 and 60 min for the mixture of CsI and SnI_2 and SnI_2 , to examine whether humidity has any effects on the phase evolution during the grinding. XRD and PL tests were performed to analyze the asprepared powders. The results are shown in Fig. S6 in Supplementary Information. The XRD patterns in Fig. S6a and c indicate that the humidity change from 40% to 60% does not cause phase differences between the as-prepared powders from the grinding of the mixture of CsI and SnI_2 and between the as-prepared powders from the mixture of CsI and SnI_2 . It is interesting to note that $CsSnCl_3$ powders of both cubic and monoclinic structures were formed from the grinding of the mixture of CsI and $SnCl_2$ at the humidity of 40% in contrast to $CsSnCl_3$ powders of cubic phase formed at the humidity of 60%, as shown in Fig. S6e. Even

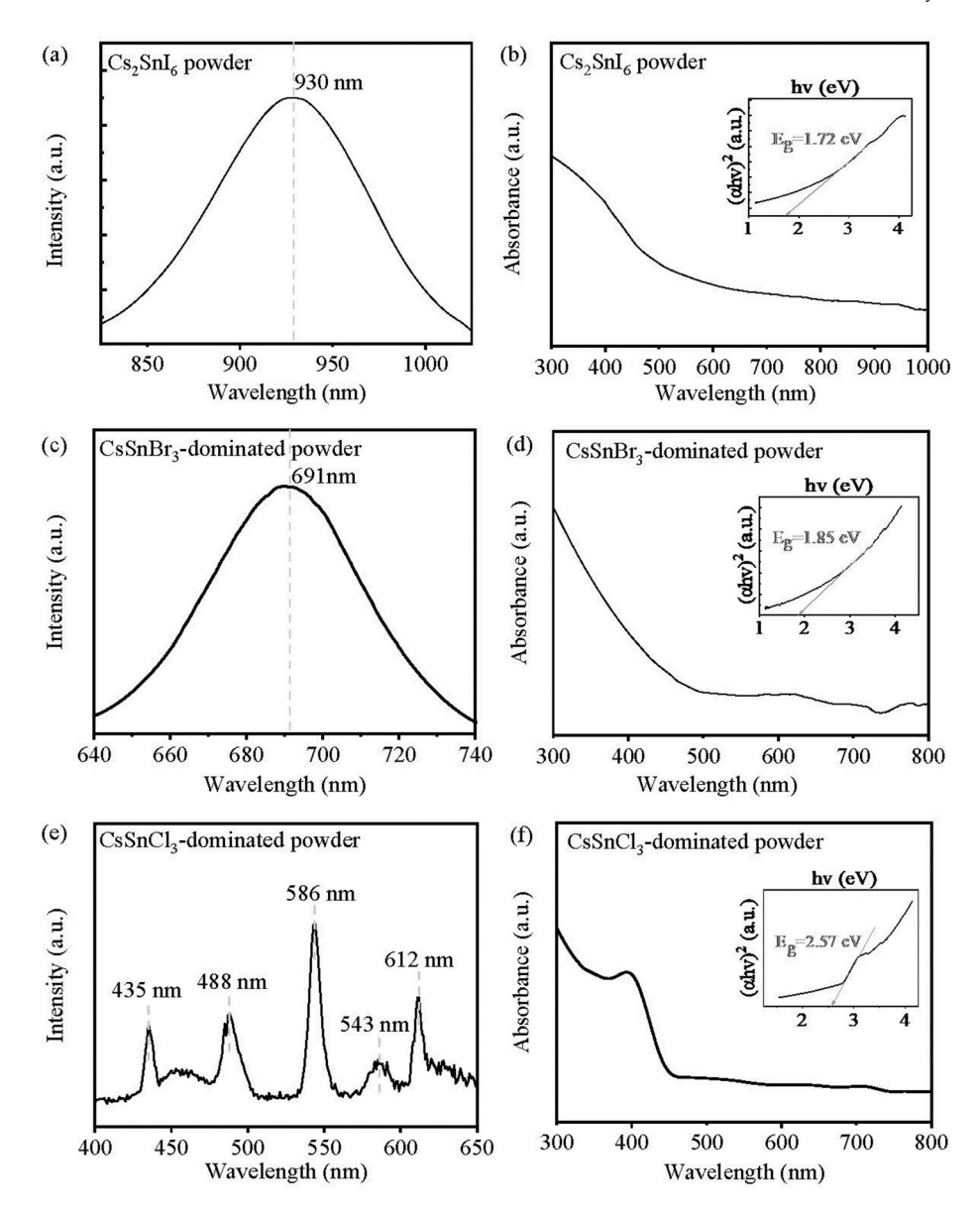


Fig. 4. PL and absorbance spectra of the as-prepared Sn-based perovskite powders: (a,b) Cs₂SnI₆ powders; (c,d) CsSnBr₃-dominated powders; and (e,f) CsSnCl₃-dominated powders. The insets in (b), (d) and (f) are the Tauc plots from the corresponding absorbance data.

though the CsSnCl₃ powders comprise of both cubic and monoclinic phases, the cubic phase is the dominant one. The PL spectra (Fig. S6b and d) of the Cs₂SnI₆ and CsSnBr₃ powders formed at the humidity of 40% are in accord with the corresponding ones formed at the humidity of 60% (Fig. 4a and c). The CsSnCl₃ powders formed at the humidity of 40% exhibit a PL peak centered at 452 nm (Fig. S6f), which is different from the corresponding one formed at the humidity of 60% (Fig. 4e). Such a difference reveals the possible effects of humidity on the evolution of phases during the grinding of the mixture of CsCl and SnCl₂.

The long-term PL stability of the stabilized phases of Cs_2SnI_6 and Cs_2SnBr_6 powders, which were stabilized in ambient conditions over a span of four to five weeks, was further examined over an additional period of 1 month in ambient conditions. As shown in Fig. 5a–b, the PL intensity retains 86.4% and 88.42% of original intensities after 1 month for the stabilized Cs_2SnI_6 and Cs_2SnBr_6 powders, respectively. There is no shift of the emission wavelength for the Cs_2SnI_6 powders, which remains at 930 nm after one month. This result indicates that the stabilized Cs_2SnI_6 powders prepared by the MC method have good optical stability. However, the stabilized Cs_2SnBr_6 powders exhibited a slight blue shift of 1 nm for the emission wavelength after one month. Fig. 5c–d presents

the variation of the PL intensity with temperature for the stabilized Cs_2SnI_6 and Cs_2SnBr_6 powders, respectively. It is evident that the PL intensity decreases with the increase of temperature for both the powders (from room temperature to 93 °C for the stabilized Cs_2SnI_6 powders and from 20 to 110 °C for the stabilized Cs_2SnBr_6 powders). There are blue shifts of 19 nm and 8 nm for the stabilized Cs_2SnI_6 and Cs_2SnBr_6 powders, respectively, for the corresponding changes in temperature. Note that the broad bands of the PL peak shown in Fig. 5a–b can be attributed to a large range of the particle (microcrystal) sizes of the asprepared powders. It needs to be pointed out that the as-prepared Cs_2SnCl_6 powders did not emit any light under the laser of 785 nm in wavelength. We performed the absorption measurement to analyze the optical characteristics of the as-prepared Cs_2SnCl_6 powders. Figure S7 presents the absorbance spectrum of the as-prepared Cs_2SnCl_6 powders, which displays an absorption peak around \sim 380 nm.

It is known that the intensity of the emission light as a function of temperature can be expressed as [48].

$$I(T) = \frac{I_0}{Ae^{(-E_a/k_BT)} + 1}$$
 (15)

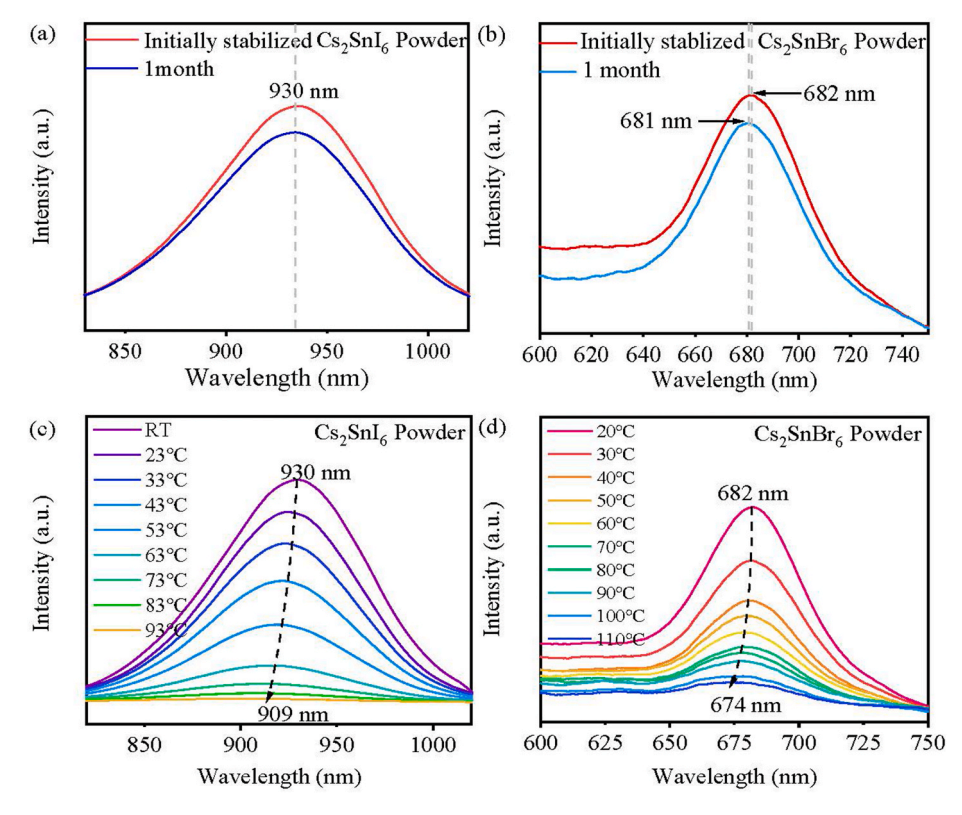


Fig. 5. Long-term PL stability of the stabilized phases of (a) Cs₂SnI₆ and (b) Cs₂SnBr₆. Thermal stability of the stabilized phases of (c) Cs₂SnI₆ and (d) Cs₂SnBr₆.

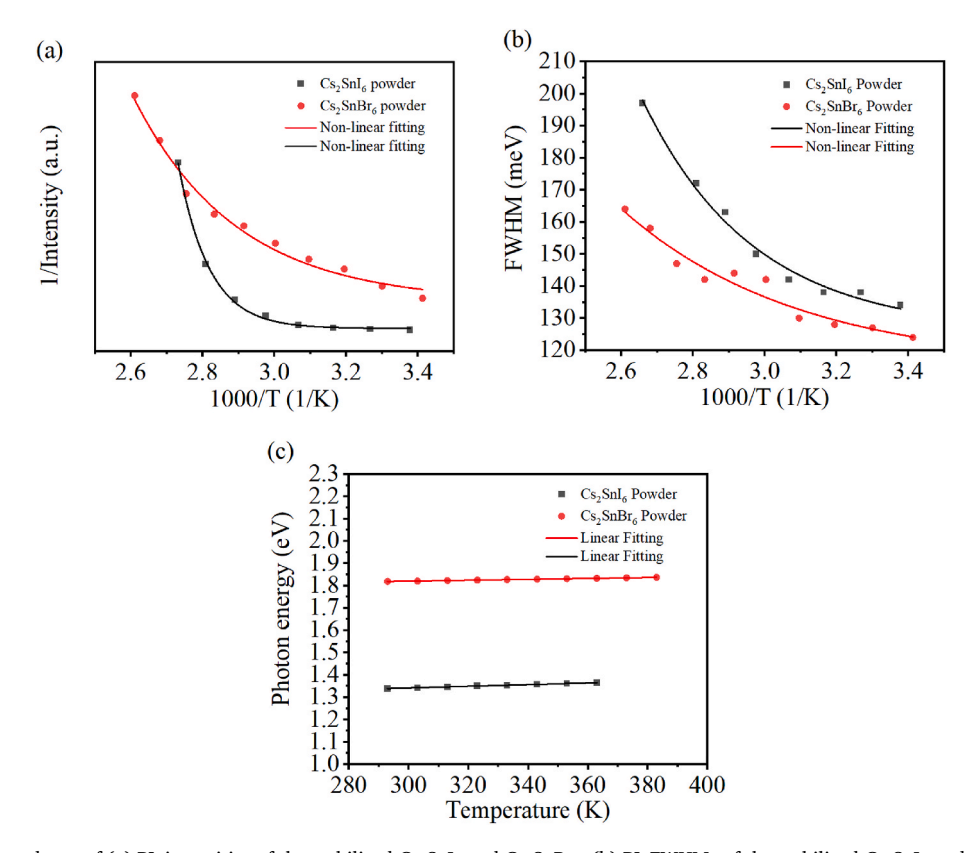


Fig. 6. Temperature dependence of (a) PL intensities of the stabilized Cs_2SnI_6 and Cs_2SnBr_6 , (b) PL FWHMs of the stabilized Cs_2SnI_6 and Cs_2SnBr_6 , and (c) photon energies of the stabilized Cs_2SnI_6 and Cs_2SnI_6 and Cs_2SnI_6 .

where I_0 is the intensity of the emission light at 0 K, E_a is the activation energy, k_B is the Boltzmann constant, and A is a constant. Using Eq. (15) to curve-fit the experimental data shown in Fig. 6a, we obtain E_a as 1005.02 and 299.53 meV for the stabilized Cs_2SnI_6 and Cs_2SnBr_6 powders, respectively. For comparison, the fitting curves are included in Fig. 6a. Such large activation energies can be attributed to the role of thermal quenching [49–52]. Note that there exists a large difference between the activation energies of the stabilized Cs_2SnI_6 and Cs_2SnBr_6 powders, suggesting the dependence of thermal quenching on chemical composition of halide perovskites.

According to the Boson model, the FWHM of a PL peak as a function of temperature can be expressed as [53].

$$\Gamma(T) = \Gamma_0 + \sigma T + \frac{\Gamma_{op}}{e^{h\omega_{op}/k_BT} - 1}$$
(16)

Here, Γ_0 is the contribution of inhomogeneous broadening, σ represents the interaction of exciton-acoustic phonon, Γ_{op} represents the contribution of the exciton-optical phonon interaction to the broadening of line width, and $h\omega_{op}$ is the energy of optical phonon. Using Eq. (16) with $\Gamma_0=0$ and $\sigma=0$ to fit the experimental data in Fig. 6b, we obtain $(\Gamma_{op},h\omega_{op})$ in the units of (meV, meV) to be (348.20, 33.81) and (9.569, 1.92) for the stabilized Cs_2SnI_6 and Cs_2SnI_6 powders, respectively. These results suggest that the Cs_2SnI_6 powder has a larger PL peak-width broadening than the Cs_2SnI_6 powder and the exciton-optical phonon interaction contributes more to the peak-width broadening of the Cs_2SnI_6 powders than the Cs_2SnI_6 powders. This is likely due to the larger optical phonon energy $(h\omega_{op})$ of the Cs_2SnI_6 powders than the Cs_2SnI_6 powders.

Fig. 6c depicts the variation of the photon energy, as calculated from the emission wavelength of the PL peak, of the emission light of the stabilized Cs_2SnI_6 and Cs_2SnB_6 powders with temperature. Increasing temperature leads to the increase of the photon energy of the emission light for both the stabilized Cs_2SnI_6 and Cs_2SnBr_6 powders, which is qualitatively in accord with the trend reported by Wu et al. [53] Note

that the photon energy of the emission light is a linearly increasing function of temperature for the temperature range used in this work. The increasing rates of the photon energy of the emission light per unit of temperature (K) are found to be 0.37 and 0.20 meV K^{-1} for the stabilized Cs_2SnI_6 and Cs_2SnBr_6 powders, respectively. Such results demonstrate that the Cs_2SnBr_6 powder has a better thermal stability than the Cs_2SnI_6 powder, as expected.

The long-term structural stability of the stabilized Sn-based perovskites was analyzed over four weeks in ambient conditions. Fig. 7a–c shows the XRD patterns of the stabilized Cs_2SnI_6 , Cs_2SnBr_6 and Cs_2SnCl_6 powders, respectively, at four different times. It is evident that there are no observable changes in the XRD patterns over the span of four weeks, indicating excellent structural stability of the MC-processed Sn-based perovskite powders.

5. Summary

In summary, we have demonstrated the feasibility of synthesizing Snbased halide perovskites via a green, mechanochemical method in an ambient environment, and revealed the phase evolutions during and after the mechanochemical processing. The freshly prepared CsSn₂Br₅ powders went through the phase evolutions to CsSnBr₃ and Cs₂SnBr₆ in 1 h and the stable phase of Cs₂SnBr₆ was obtained from CsSnBr₃ and Cs₂SnBr₆ after 28 days. The Cs₂SnCl₄ powders went through the phase evolution to CsSnCl3 in 1 h, and the stable phase of Cs2SnCl6 was achieved after 36 days from both Cs2SnCl4 and CsSnCl3. The as-prepared Cs₂SnI₆ is the stable phase. All the stabilized Cs₂SnI₆, Cs₂SnBr₆ and Cs₂SnCl₆ powders exhibited excellent long-term structural stability, which can be attributed to the presence of Sn⁴⁺. The long-term PL tests reveal that the stabilized Cs₂SnI₆ and Cs₂SnBr₆ powders retained 86.4% and 88.42% of original PL intensities after one month. The results of both the long-term XRD and PL tests suggest that the Sn-based perovskite powders prepared by the mechanochemical processing of the precursor powders possess good structural and optical stabilities. The temperature-dependence of the stabilized Cs₂SnI₆ and Cs₂SnBr₆

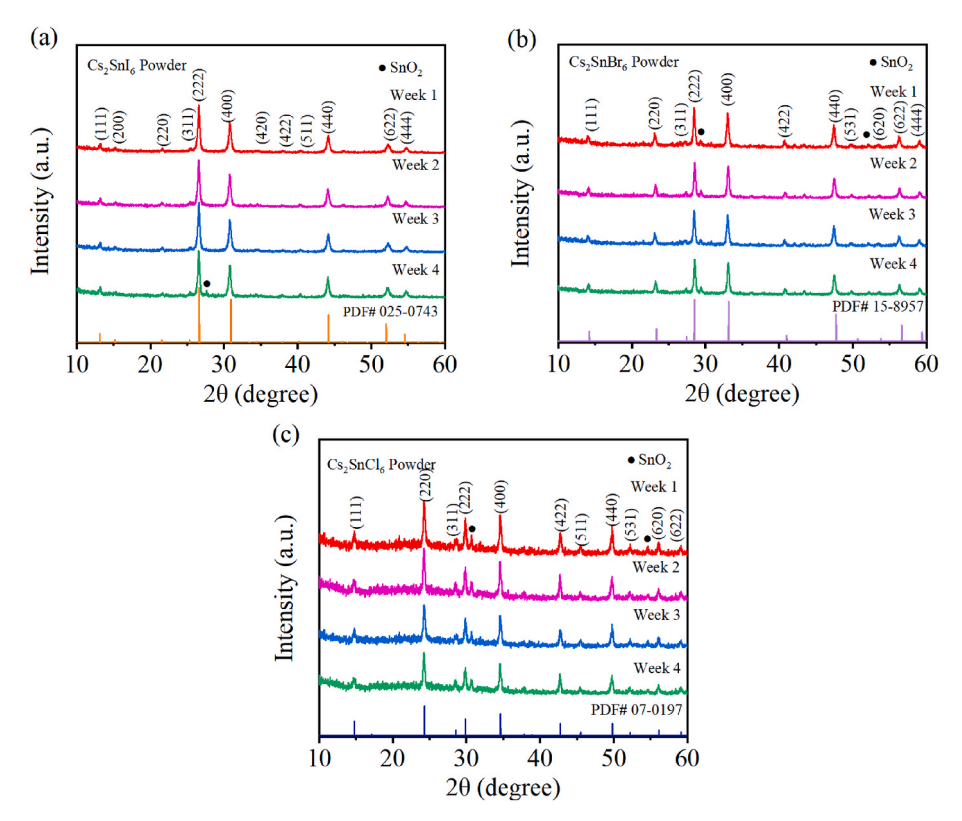


Fig. 7. XRD patterns of the stabilized phases of (a) Cs₂SnI₆, (b) Cs₂SnBr₆ and (c) Cs₂SnCl₆ at different instants.

indicates that the Cs₂SnBr₆ powders have better thermal stability than the Cs₂SnI₆ powders.

CRediT authorship contribution statement

Xuan Huang: Data curation, Formal analysis, Investigation, Methodology, Writing - original draft. Xiaobing Tang: Data curation, Formal analysis, Investigation, Methodology, Validation, Writing - original draft, Writing - review & editing. Xiyu Wen: Data curation, Methodology. Y. Charles Lu: Funding acquisition, Project administration, Supervision, Writing - review & editing. Fuqian Yang: Conceptualization, Funding acquisition, Methodology, Project administration, Resources, Supervision, Writing - review & editing.

Declaration of competing interest

The authors declare that they have no known competing financial interests or personal relationships that could have appeared to influence the work reported in this paper.

Data availability

Data will be made available on request.

Acknowledgments

FY is grateful for the support by the NSF through the grant CMMI-1854554, monitored by Drs. Khershed Cooper and Thomas Francis Kuech, and CBET- 2018411 monitored by Dr. Nora F Savage.

Appendix A. Supplementary data

Supplementary data to this article can be found online at https://doi.org/10.1016/j.jlumin.2023.120432.

References

- [1] A. Dutta, R.K. Behera, P. Pal, S. Baitalik, N. Pradhan, Near-unity photoluminescence quantum efficiency for all CsPbX₃ (X= Cl, Br, and I) perovskite nanocrystals: a generic synthesis approach, Angew. Chem. Int. Ed. 58 (2019)
- [2] A. Swarnkar, R. Chulliyil, V.K. Ravi, M. Irfanullah, A. Chowdhury, A. Nag, Colloidal CsPbBr₃ perovskite nanocrystals: luminescence beyond traditional quantum dots, Angew. Chem. 127 (2015) 15644–15648.
- [3] C.-Y. Huang, C.-C. Wu, C.-L. Wu, C.-W. Lin, CsPbBr₃ perovskite powder, a robust and mass-producible single-source precursor: synthesis, characterization, and optoelectronic applications, ACS Omega 4 (2019) 8081–8086.
- [4] X. Tang, Y. Zhang, N.L. Kothalawala, X. Wen, D.Y. Kim, F. Yang, MAPbBr₃ nanocrystals from aqueous solution for poly (methyl methacrylate)-MAPbBr₃ nanocrystal films with compression-resistant photoluminescence, Nanotechnology 33 (2022) 235605.
- [5] Z. Yang, Q. Xu, X. Wang, J. Lu, H. Wang, F. Li, L. Zhang, G. Hu, C. Pan, Large and ultrastable all-inorganic CsPbBr₃ monocrystalline films: low-temperature growth and application for high-performance photodetectors, Adv. Mater. 30 (2018) 1802110.
- [6] L. Protesescu, S. Yakunin, M.I. Bodnarchuk, F. Krieg, R. Caputo, C.H. Hendon, R. X. Yang, A. Walsh, M.V. Kovalenko, Nanocrystals of cesium lead halide perovskites (CsPbX₃, X= Cl, Br, and I): novel optoelectronic materials showing bright emission with wide color gamut, Nano Lett. 15 (2015) 3692–3696.
- [7] X. Li, Y. Wu, S. Zhang, B. Cai, Y. Gu, J. Song, H. Zeng, CsPbX₃ quantum dots for lighting and displays: room-temperature synthesis, photoluminescence superiorities, underlying origins and white light-emitting diodes, Adv. Funct. Mater. 26 (2016) 2435–2445.
- [8] X. Zhang, W. Wang, B. Xu, S. Liu, H. Dai, D. Bian, S. Chen, K. Wang, X.W. Sun, Thin film perovskite light-emitting diode based on CsPbBr₃ powders and interfacial engineering, Nano Energy 37 (2017) 40–45.
- [9] C.C. Lin, A. Meijerink, R.-S. Liu, Critical red components for next-generation white LEDs, J. Phys. Chem. Lett. 7 (2016) 495–503.
- [10] F. Palazon, F. Di Stasio, Q.A. Akkerman, R. Krahne, M. Prato, L. Manna, Polymer-free films of inorganic halide perovskite nanocrystals as UV-to-white color-conversion layers in LEDs, Chem. Mater. 28 (2016) 2902–2906.
 [11] J. Song, J. Li, X. Li, L. Xu, Y. Dong, H. Zeng, Quantum dot light-emitting diodes
- [11] J. Song, J. Li, X. Li, L. Xu, Y. Dong, H. Zeng, Quantum dot light-emitting diodes based on inorganic perovskite cesium lead halides (CsPbX₃), Adv. Mater. 27 (2015) 7162–7167.

- [12] F. Giustino, H.J. Snaith, Toward lead-free perovskite solar cells, ACS Energy Lett. 1 (2016) 1233–1240.
- [13] H. Wei, T. Si, F. Xu, W. Fan, T. Yang, B. Cao, F. Juan, J. Xu, Y. Wu, Enhanced photoluminescence of double perovskite Cs₂SnI₆ nanocrystals via Na plus doping, Opt Express 31 (2023) 25298–25306.
- [14] L. Zhou, L. Zhang, H. Li, W. Shen, M. Li, R. He, Defect passivation in air-stable tin (IV)-halide single crystal for emissive self-trapped excitons, Adv. Funct. Mater. 31 (2021) 2108561.
- [15] Z. Ma, Z. Shi, D. Yang, Y. Li, F. Zhang, L. Wang, X. Chen, D. Wu, Y. Tian, Y. Zhang, L. Zhang, X. Li, C. Shan, High color-rendering index and stable white light-emitting diodes by assembling two broadband emissive self-trapped excitons, Adv. Mater. 33 (2021) 2001367.
- [16] F. Zhang, Z. Zhao, B. Chen, H. Zheng, L. Huang, Y. Liu, Y. Wang, A.L. Rogach, Strongly emissive lead-free 0D Cs₃Cu₂I₅ perovskites synthesized by a room temperature solvent evaporation crystallization for down-conversion light-emitting devices and fluorescent inks, Adv. Opt. Mater. 8 (2020) 1901723.
- [17] T. Jiang, J. Wang, L. Xie, C. Bai, M. Wang, Y. Wu, F. Zhang, Y. Zhao, B. Chen, Y. Wang, In situ fabrication of lead-free Cs₃Cu₂I₅ nanostructures embedded in poly (vinylidene fluoride) electrospun fibers for polarized emission, ACS Appl. Nano Mater. 5 (2022) 508–516.
- [18] L. Xie, B. Chen, F. Zhang, Z. Zhao, X. Wang, L. Shi, Y. Liu, L. Huang, R. Liu, B. Zou, Y. Wang, Highly luminescent and stable lead-free cesium copper halide perovskite powders for UV-pumped phosphor-converted light-emitting diodes, Photon. Res. 8 (2020) 768–775.
- [19] L. Chao, T. Niu, W. Gao, C. Ran, L. Song, Y. Chen, W. Huang, Solvent engineering of the precursor solution toward large-area production of perovskite solar cells, Adv. Mater. 33 (2021) 2005410.
- [20] C. Liu, Y.-B. Cheng, Z. Ge, Understanding of perovskite crystal growth and film formation in scalable deposition processes, Chem. Soc. Rev. 49 (2020) 1653–1687.
- [21] J. Wu, X. Xu, Y. Zhao, J. Shi, Y. Xu, Y. Luo, D. Li, H. Wu, Q. Meng, DMF as an additive in a two-step spin-coating method for 20% conversion efficiency in perovskite solar cells, ACS Appl. Mater. Interfaces 9 (2017) 26937–26947.
- [22] C. de Mello Donegá, P. Liljeroth, D. Vanmaekelbergh, Physicochemical evaluation of the hot-injection method, a synthesis route for monodisperse nanocrystals, Small 1 (2005) 1152–1162.
- [23] R.I. Walton, Perovskite oxides prepared by hydrothermal and solvothermal synthesis: a review of crystallisation, chemistry, and compositions, Chem. Eur J. 26 (2020) 9041–9069.
- [24] Y. Vaynzof, The future of perovskite photovoltaics—thermal evaporation or solution processing? Adv. Energy Mater. 10 (2020) 2003073.
- [25] J. Luo, X. Wang, S. Li, J. Liu, Y. Guo, G. Niu, L. Yao, Y. Fu, L. Gao, Q. Dong, Efficient and stable emission of warm-white light from lead-free halide double perovskites, Nature 563 (2018) 541–545.
- [26] F. Igbari, Z.K. Wang, L.S. Liao, Progress of lead-free halide double perovskites, Adv. Energy Mater. 9 (2019) 1803150.
- [27] R.T. O'Neill, R. Boulatov, The many flavours of mechanochemistry and its plausible conceptual underpinnings, Nat. Rev. Chem 5 (2021) 148–167.
- [28] X. Liu, Y. Li, L. Zeng, X. Li, N. Chen, S. Bai, H. He, Q. Wang, C. Zhang, A review on mechanochemistry: approaching advanced energy materials with greener force, Adv. Mater. 34 (2022) e2108327.
- [29] L. Takacs, The historical development of mechanochemistry, Chem. Soc. Rev. 42 (2013) 7649–7659.
- [30] A.D. Jodlowski, A. Yépez, R. Luque, L. Camacho, G. de Miguel, Benign-by-design solventless mechanochemical synthesis of three-, two-, and one-dimensional hybrid perovskites, Angew. Chem. Int. Ed. 55 (2016) 14972–14977.
- [31] A. Karmakar, M.S. Dodd, X. Zhang, M.S. Oakley, M. Klobukowski, V.K. Michaelis, Mechanochemical synthesis of 0D and 3D cesium lead mixed halide perovskites, Chem. Commun. 55 (2019) 5079–5082.
- [32] K. Manukyan, A. Yeghishyan, D. Moskovskikh, J. Kapaldo, A. Mintairov, A. Mukasyan, Mechanochemical synthesis of methylammonium lead iodide perovskite, J. Mater. Sci. 51 (2016) 9123–9130.
- [33] Z. Hong, D. Tan, R.A. John, Y.K.E. Tay, Y.K.T. Ho, X. Zhao, T.C. Sum, N. Mathews, F. Garcia, H.S. Soo, Completely solvent-free protocols to access phase-pure, metastable metal halide perovskites and functional photodetectors from the precursor salts, iScience 16 (2019) 312–325.
- [34] Y. El Ajjouri, F. Locardi, M.C. Gelvez-Rueda, M. Prato, M. Sessolo, M. Ferretti, F. C. Grozema, F. Palazon, H.J. Bolink, Mechanochemical synthesis of Sn(II) and Sn (IV) iodide perovskites and study of their structural, chemical, thermal, optical, and electrical properties, Energy Technol. 8 (2020) 1900788.
- [35] J.G. Osorio, F.J. Muzzio, Evaluation of resonant acoustic mixing performance, Powder Technol. 278 (2015) 46–56.
- [36] C. Mottillo, Y. Lu, M.-H. Pham, M.J. Cliffe, T.-O. Do, T. Friscic, Mineral neogenesis as an inspiration for mild, solvent-free synthesis of bulk microporous metal-organic frameworks from metal (Zn, Co) oxides, Green Chem. 15 (2013) 2121–2131.
- [37] F. Qi, R.S. Stein, T. Friscic, Mimicking mineral neogenesis for the clean synthesis of metal-organic materials from mineral feedstocks: coordination polymers, MOFs and metal oxide separation, Green Chem. 16 (2014) 121–132.
- [38] J.C.-R. Ke, D.J. Lewis, A.S. Walton, B.F. Spencer, P. O'Brien, A.G. Thomas, W. R. Flavell, Ambient-air-stable inorganic Cs₂SnI₆ double perovskite thin films via aerosol-assisted chemical vapour deposition, J. Mater. Chem. A 6 (2018) 11205–11214.
- [39] A. Wang, X. Yan, M. Zhang, S. Sun, M. Yang, W. Shen, X. Pan, P. Wang, Z. Deng, Controlled synthesis of lead-free and stable perovskite derivative Cs₂SnI₆ nanocrystals via a facile hot-injection process, Chem. Mater. 28 (2016) 8132–8140.
- [40] A.E. Maughan, A.M. Ganose, M.M. Bordelon, E.M. Miller, D.O. Scanlon, J. R. Neilson, Defect tolerance to intolerance in the vacancy-ordered double

- perovskite semiconductors Cs₂SnI₆ and Cs₂TeI₆, J. Am. Chem. Soc. 138 (2016)
- [41] L. Xu, P. Wang, Y. Kang, X. Zhang, M. Chen, Q. Wu, C. Sun, Z. Qiao, Z. Lin, Structural, electronic, and optical properties of Cs₂SnX₄ (X = Cl, Br, and I) multilayers: a density functional theory study, Phys. Status Solidi B 260 (2023) 2200220
- [42] J.-M. Heo, H. Cho, S.-C. Lee, M.-H. Park, J.S. Kim, H. Kim, J. Park, Y.-H. Kim, H. J. Yun, E. Yoon, Bright lead-free inorganic CsSnBr₃ perovskite light-emitting diodes, ACS Energy Lett. 7 (2022) 2807–2815.
- [43] L. Cao, S.-M. Gu, B. Liu, L. Huang, J. Zhang, Y. Zhu, J. Wang, Highly ambient stable CsSnBr₃ perovskite via a new facile room-temperature "coprecipitation" strategy, ACS Appl. Mater. Interfaces 15 (2023) 30409–30416.
- [44] M.S. Ali, S. Das, Y.F. Abed, M.A. Basith, Lead-free CsSnCl₃ perovskite nanocrystals: rapid synthesis, experimental characterization and DFT simulations, Phys. Chem. Chem. Phys. 23 (2021) 22184–22198.
- [45] D.E. Scaife, P.F. Weller, W.G. Fisher, Crystal preparation and properties of cesium tin(II) trihalides, J. Solid State Chem. 9 (1974) 308–314.
- [46] X. Qiu, B. Cao, S. Yuan, X. Chen, Z. Qiu, Y. Jiang, Q. Ye, H. Wang, H. Zeng, J.J.S.E. M. Liu, From unstable CsSnI₃ to air-stable Cs₂SnI₆: a lead-free perovskite solar cell light absorber with bandgap of 1.48 eV and high absorption coefficient, Sol. Energy Mater. Sol. Cell. 159 (2017) 227–234.

- [47] G.-R. Chang, F. Ma, D.-Y. Ma, K.-W. Xu, Multi-band silicon quantum dots embedded in an amorphous matrix of silicon carbide, Nanotechnology 21 (2010) 465605.
- [48] S. Sun, T. Salim, N. Mathews, M. Duchamp, C. Boothroyd, G. Xing, T.C. Sum, Y. M. Lam, The origin of high efficiency in low-temperature solution-processable bilayer organometal halide hybrid solar cells, Energy Environ. Sci. 7 (2014) 399–407.
- [49] X. Tang, N.L. Kothalawala, Y. Zhang, D. Qian, D.Y. Kim, F. Yang, Water-driven CsPbBr₃ nanocrystals and poly (methyl methacrylate)-CsPbBr₃ nanocrystal films with bending-endurable photoluminescence, Chem. Eng. J. 425 (2021) 131456.
- [50] M. Tangi, P. Mishra, B. Janjua, A. Prabaswara, C. Zhao, D. Priante, J.-W. Min, T. K. Ng, B.S. Ooi, Role of quantum-confined Stark effect on bias dependent photoluminescence of N-polar GaN/InGaN multi-quantum disk amber light emitting diodes, J. Appl. Phys. 123 (2018) 105702.
- [51] D. Bimberg, M. Sondergeld, E. Grobe, Thermal dissociation of excitons bounds to neutral acceptors in high-purity GaAs, Phys. Rev. B 4 (1971) 3451–3454.
- [52] J. Grandal, J. Pereiro, A. Bengoechea-Encabo, S. Fernandez-Garrido, M.A. Sanchez-Garcia, E. Munoz, E. Calleja, E. Luna, A. Trampert, InN/InGaN multiple quantum wells emitting at 1.5 μm grown by molecular beam epitaxy, Appl. Phys. Lett. 98 (2011) 061901.
- [53] K. Wu, A. Bera, C. Ma, Y. Du, Y. Yang, L. Li, T. Wu, Temperature-dependent excitonic photoluminescence of hybrid organometal halide perovskite films, Phys. Chem. Chem. Phys. 16 (2014) 22476–22481.